Aalborg Universitet

Design of a Triple-Band Shared-Aperture Antenna with High Figures of Merit

Mei, Peng; Lin, Xian Qi ; Pedersen, Gert Frølund; Zhang, Shuai

Design of A Triple-Band Shared-Aperture Antenna with High Figures of Merit

Peng Mei, *Student Member, IEEE*, Xian Qi Lin, *Senior Member, IEEE*, Gert Frølund Pedersen, *Member, IEEE,* and Shuai Zhang, *Senior Member, IEEE*

Abstract— **This communication develops a triple-band shared-aperture antenna operating at X/K/Ka-band with high figures of merit such as high aperture reuse efficiency, simple configuration to achieve high gain. The proposed antenna is implemented by integrating a Fabry-Perot (FP) cavity antenna operating at X-band into a dual-band reflectarray antenna enabled by frequency selective surfaces (FSSs). The unit cells (UCs) to form the phase-shifting surfaces for the dual-band reflectarray antenna can offer partial reflectance/transmission abilities at X-band simultaneously, thereby enabling the implementation of a FP cavity antenna. The frequency responses of the proposed antenna are highly independent at X/K/Ka-band, which facilitates the design and optimization. For demonstration, a prototype has been described, fabricated, and measured. The simulated results present 3-dB gain bandwidths of 11.2 % (8.4 to 9.4 GHz), 10.0% (24 to 26.6 GHz), and 13.3% (35 to 40 GHz), which are all experimentally verified. The measured results also present a peak gain of 16.8 dBi at 9.0 GHz, 23.8 dBi at 26 GHz, and 26.7 dBi at 38 GHz.**

Index Terms— **Triple-band, shared-aperture, high aperture reuse efficiency, Fabry-Perot antenna, reflectarray antenna.**

I. INTRODUCTION

A shared-aperture antenna is a kind of antenna that typically combines multiple antennas in an efficient architecture to make all sub-antennas radiation through a shared aperture. Shared-aperture antennas, therefore, feature high space reuse efficiencies and multiband for multiservice applications, attracting lots of attention and interest in wireless communications.

The past few years have witnessed the developments and progress of shared-aperture antennas [1]-[13]. Most of the reported literature mainly focused on implementations of dual-band shared-aperture antennas [1]-[10]. A straightforward approach to realize a dual-band shared-aperture antenna is to interleave two patch antenna arrays with different sizes in the same aperture as reported in [1],[2], where two feeding networks are needed accordingly to excite the two antenna arrays. This approach is, however, not suitable for large-scale antenna arrays since the feeding networks would be very complicated and their losses would be high as well, especially at the millimeter-wave bands. Subsequently, other types of antennas are attempted to design shared-aperture antennas. Among them, a slot antenna (array) is one of the widely used sub-antennas, which usually operates at the millimeter-wave band [3]-[6]. The main drawback of a slot antenna (array) lies in its difficulties in the realization of dual-polarization for the corresponding shared-aperture antenna. In [7], Chen *et al.* proposed a dual-polarized shared-aperture antenna by stacking dipole antennas operated at 600-900 MHz and 3.5-4.9 GHz, where the dipole array operating at the high-frequency band was located above the one operating at the low-frequency band with a certain separation. The stacking configuration makes full use of the space but is not suitable at

the millimeter-wave band.

One of the considerations in a shared-aperture antenna design is its number of operating bands. From the practical application viewpoint, a shared-aperture antenna covering as many as possible different bands is preferred for multiservice applications. To the authors' best knowledge, there is rare literature to report triple-band shared-aperture antennas [11]-[13] since it is challenging to find out three sub-antennas and combine them efficiently to radiate through the same aperture. In [11], [12], the authors achieved triple-band and dual-polarized shared-aperture antenna by employing the conventional approach used in [1],[2]. It could be observed that feeding networks were much more complicated. The stacking configuration used in [7] was also expanded to design a triple-band shared-aperture antenna operated at sub-6GHz as reported in [13].

This communication proposed a design methodology that is distinguished from the techniques described in [11]-[13] to achieve a triple-band shared-aperture antenna with high figures of merit, such as high aperture reuse efficiency, simple configuration to achieve high gain. The methodology is inspired by dual-band reflectarray antennas [9], [10], [14], [15] and Fabry-Perot (FP) cavity antennas [8], [16], [17], where a FP cavity antenna can be properly integrated into a dual-band reflectarray antenna. For demonstration, a triple-band shared-aperture antenna operated at X/K/Ka-band has been described, fabricated, and measured. The FP cavity is designed to work from 8.25 to 9.4 GHz, while the operating bands of the dual-band reflectarray antenna are 24 to 28 GHz and 35 to 40 GHz, respectively. Besides, the proposed antenna is possible to realize dual/circular polarization if a dual-/circular-polarized feeding source is applied, since the unit cells of the design are symmetrical and polarization-insensitive. Compared to our previous work in [8], where a dual-band shared-aperture antenna was performed by combining a FP cavity antenna and a folded transmitarray antenna, the proposed shared-aperture here is triple-band, and the bandwidth of the FP cavity antenna at the low-frequency band is much wider as the bandwidth of partial reflectance/transmission of the proposed UC is wider and a matching layer is introduced to improve the impedance match. Moreover, the proposed antenna shows high independence among the three operating bands, where the operating frequencies and radiation performance can be controlled separately.

The rest of this communication is organized as follows. The UCs to construct the phase-shifting surfaces are presented in Section II. The implementation of the proposed triple-band shared-aperture antenna is given in Section III. The simulated and measured results are then given in Section IV. Finally, conclusions are drawn in Section V.

II. UNIT CELL DESIGNS AND ANALYSIS

The schematic diagram of the proposed triple-band shared-aperture antenna is presented in Fig. 1. It consists of two reflectarray antennas and a Fabry-Perot (FP) cavity antenna, where the two reflectarray antennas respectively operate at the middle- and high-frequency bands, and the FP cavity antenna works at the low-frequency band. To implement such a triple-band shared-aperture antenna, the phase-shifting surface for high frequency should satisfy the following conditions: a). phase-shifting capability at the high-frequency band; b). be transparent at the middle-frequency band; c). partial reflection/

transmission at the low-frequency band. In contrast, the phase-shifting surface for middle frequency is required to provide: a). phase-shifting ability at the middle-frequency band; b). be fully reflective at the low-frequency band. It is also preferred that the frequency responses at the low-, middle-, and high-frequency bands are highly independent so that we can control the performance at different bands separately to facilitate the design.
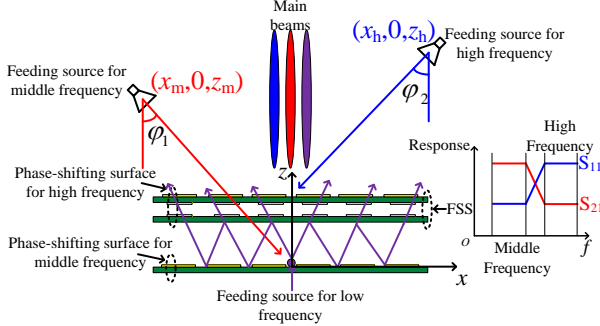

Fig. 1. The schematic diagram of the proposed triple-band and shared-aperture antenna.
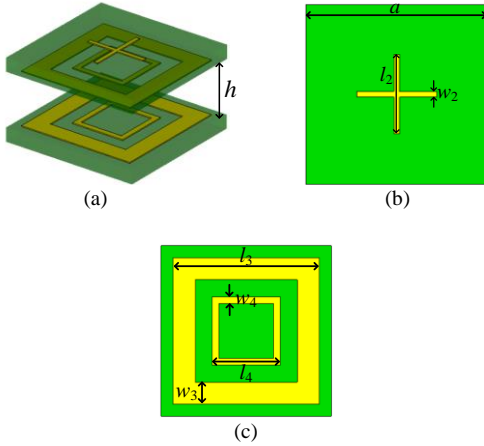

Fig.2. Geometries of the UC for implementation of phase shifting surface at the high-frequency band. (a). Perspective view (transparent) (b). Front view. (c). Front view of the FSS. (a = 5 mm, h = 2 mm, w_2 = 0.15 mm, l_3 = 4.3 mm, w_3 = 0.65 mm, l_4 = 2.0 mm, w_4 = 0.2 mm.)

A. Analysis of the UC for implementation of the phase-shifting surface at the high-frequency band

The geometries shown in Figs. 2(a) and (b) are perspective and front views of the UC for the implementation of the phase-shifting surface at the high-frequency band. This UC consists of two double-square loops and a cross-shaped dipole. Two double-square loops are printed on two substrates with a separation of h, while a cross-shaped dipole is printed on the other side of the substrate. The substrates used here are Rogers RO4003C with a dielectric constant of 3.55, a loss tangent of 0.004, and a thickness of 0.508 mm. The two-layered double-square loops act as a frequency selective surface (FSS). In this design, the dimensions of the FSS are properly decided to make it fully reflective at the high-frequency band of 35-40 GHz and transparent at the middle-frequency band of 24-28 GHz simultaneously.

The frequency responses of the UC are simulated with CST Microwave Studio Software, where the periodic boundary conditions are imposed on the UC to simulate an infinite surface to obtain the desired results. As seen in Fig. 2 (a), the UC can offer a partial reflection/transmission from 5 to 11 GHz, a bandpass response from 24 to 28 GHz, and a full reflection from 35 to 40 GHz. The full reflection implies that the FSS can act as a metal ground from 35 to 40

GHz functionally. For such a UC, the cross-shaped dipole on the substrate can be properly sized to offer desired phase shifts at the high-frequency band by varying its length.
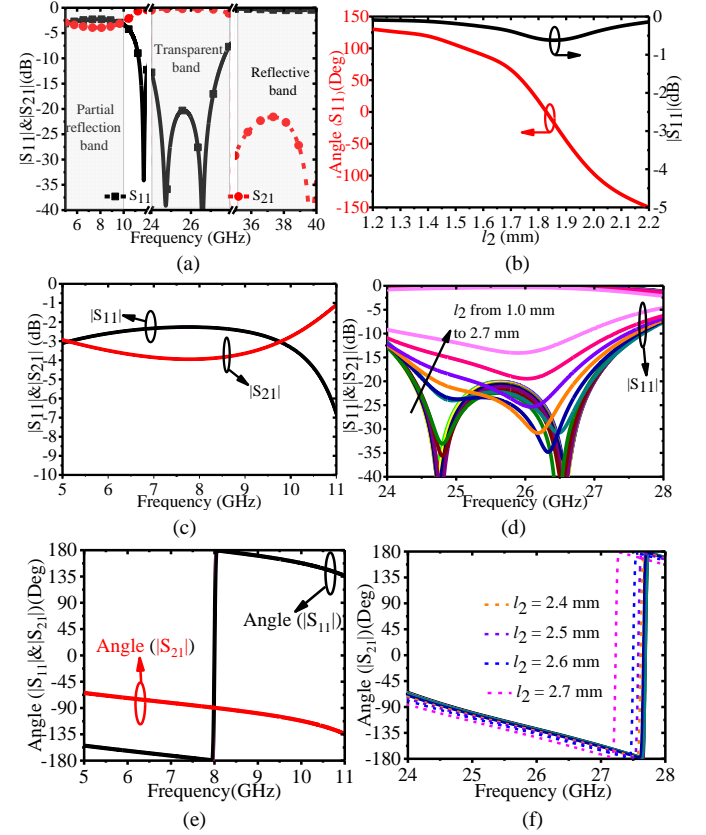

Fig. 3. Frequency responses of the UC: (a). $|S_{11}|$ and $|S_{21}|$ in three bands. (b). Reflection phase and amplitude with different l_2 at 38 GHz. (c). $|S_{11}|$ and $|S_{21}|$ from 5 to 11 GHz with l_2 varied from 1.0 to 2.7 mm. (d). $|S_{11}|$ and $|S_{21}|$ from 24 to 28 GHz with l_2 varied from 1.0 to 2.7 mm. (e). Reflection and transmission phases from 5 to 11 GHz with l_2 varied from 1.0 to 2.7 mm. (f). Transmission phase of the UC from 24 to 28 GHz with l_2 varied from 1.0 to 2.7 mm.

In order to check the effects of the cross-shaped dipole length on the UC frequency responses at low and middle frequencies, the reflection/ transmission amplitudes and phases are simulated with different values of l_2. As seen in Figs. 2(c) and (e), the frequency responses of the UC are quite stable from 5 to 11 GHz as all curves are completely overlapped when l_2 changes from 1.0 to 2.7 mm, which implies high independences that the UC can provide between the low- and high-frequency bands. Likewise, the frequency responses of the UC from 24 to 28 GHz with different l_2 are plotted in Figs. 2 (d) and (f). It is observed that $|S_{11}|$ starts to be worse when l_2 is longer than 2.4 mm. Besides, the transmission phase of the UC provides more phase delay when l_2 is larger than 2.2 mm. Specifically speaking, the transmission phase of the UC is a fixed value (-118 degree at 26 degrees for example) when l_2 is tuned from 1.0 to 2.2 mm; however, the transmission phase of the UC is varied from -118 to -135 degrees gradually when l_2 is tuned from 2.2 to 2.7 mm.

The frequency responses shown in Figs. 2 (c)-(f) also indicate that the UC is more vulnerable to be affected with different values of l_2 at the middle-frequency band, which should be avoided in the proposed triple-band shared-aperture antenna design. Here, we adopt a compromising approach that keeps l_2 less than 2.2 mm to eliminate the influences. From Fig. 3, it is found that the S-parameter at the middle-frequency band is extremely stable when l_2 is tuned from 1.2 to 2.2 mm; while within this range, the UC can offer 270 degrees

reflection phase coverage at 38 GHz as seen from Fig. 3(b). This approach, however, will sacrifice the phase-shifting abilities of the UC, resulting in a slightly degraded realized gain of the proposed antenna at the high-frequency band.

Compared to our previous work in [8], the bandwidth of the partial reflection/transmission of the proposed UC at the low-frequency band is much wider, which is mainly attributed to the two-layered UC used here while it is a four-layered one in [8]. The four-layered UC can introduce more reflection zeros at the low-frequency band to generate multiple narrow bands, resulting in the narrow bandwidth of the partial reflectance/transmission of the UC. The wider bandwidth of the proposed two-layered UC can contribute to the wide bandwidth of the FP cavity antenna, which will be demonstrated in the following.
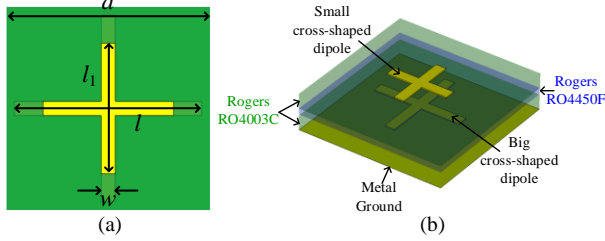

Fig.4. Geometries of the UC for implementation of phase shifting surface at the middle-frequency band. (a). Front view. (b). Perspective view (transparent). (a = 5 mm, h = 2 mm, l_1 = 0.7l, w = 0.35 mm.)
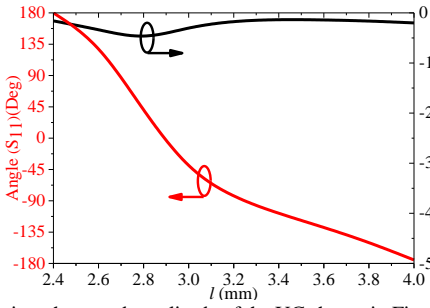

Fig. 5. Reflection phase and amplitude of the UC shown in Fig. 4 with different values of l at 26 GHz.
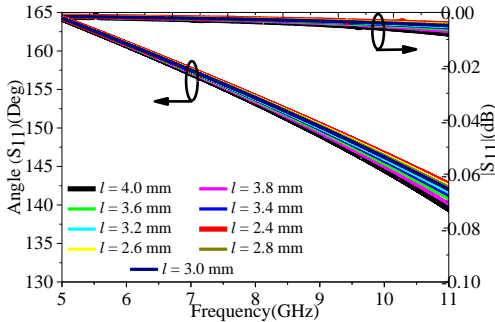

Fig. 6. Reflection phase and amplitude of the UC shown in Fig. 4 at the low-frequency band with different values of l from 5 to 12 GHz.

B. Analysis of UCs for the implementation of the phase-shifting surface at the middle-frequency band.

The geometries of the UC for the implementation of the phase-shifting surface at the middle-frequency band are shown in Fig. 4, where a short cross-shaped dipole is stacked on a long and grounded cross-shaped dipole. The length of the short cross-shaped dipole is proportional to the long one. Both the cross-shaped dipoles are printed on Rogers RO4003C substrate with a dielectric constant of 3.55, a loss tangent of 0.004, and a thickness of 0.508 mm. A bonding film made of Rogers RO4450F is sandwiched between the two substrates to firmly connect them. The Rogers RO4450F used here is with a

dielectric constant of 3.52, a loss tangent of 0.0029, and a featured thickness of 0.202 mm.

Likewise, for such a UC, the phase shifts can also be tuned by simply varying the length of the cross-shaped dipole. Fig. 5 gives the reflection phase and amplitude of the UC at 26 GHz with different values of l, where a full phase-cycle (2π) is observed and the reflection loss is less than 0.5 dB when l is tuned from 2.4 to 4.0 mm.

The reflection phase and amplitude of the UC at the low-frequency band are also examined with different values of l. As seen in Fig. 6, a full reflectance can be observed from 5 to 11 GHz with different l, where at 5 and 11 GHz the reflection amplitude difference is 0.00027 and 0.00517 dB, respectively, while the reflection phase difference is around 0.12 and 3.0 degrees, respectively. Fig. 6 also indicates good independence of the UC at low and middle frequencies.
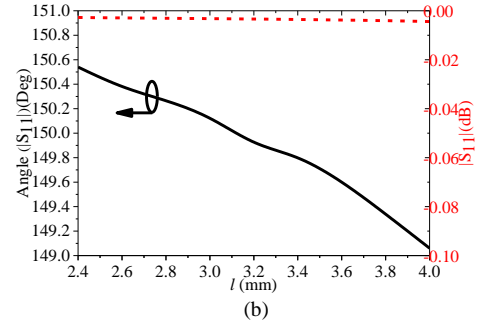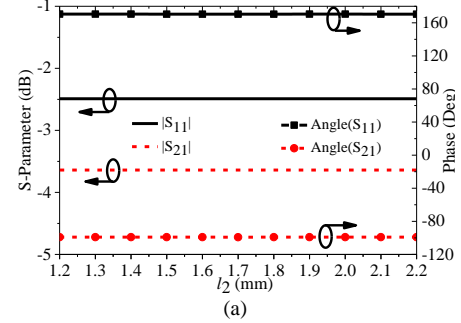

Fig. 7. Phases and amplitudes of the UCs. (a). Reflection/transmission amplitudes and phases at 9.0 GHz from Figs. 3 (c) and (f). (b). Reflection amplitude and phase at 9.0 GHz from Fig. 6

C. Analysis of the frequency response at the low-frequency band.

The phase-shifting surfaces for the middle and high-frequency bands should also satisfy the conditions to form a FP cavity antenna as seen in Fig. 1. As is known to all, the superstrate and metal ground for a FP cavity antenna are usually uniform and homogenous so that they can provide the same reflection/transmission amplitudes and reflections at any point on them to make the electric field on the aperture of the superstrate in phase, leading to a high gain. However, since the UCs constituting the phase-shifting surfaces are not physically identical, their reflection/transmission amplitudes and phases should be examined with different dimensions at the low-frequency band to check their feasibilities to implement a FP cavity antenna.

We extract the reflection/transmission amplitudes and phases at 9 GHz from Figs. 3(c) and (f) to plot their relations with different l_2 as shown in Fig. 7(a), it is observed that the reflection/transmission amplitudes and phases can keep the same when l_2 varies from 1.2 to 2.2 mm. Likewise, the reflection amplitude and phase at 9 GHz are also extracted from Fig. 6 and plotted with different values of l as shown in Fig. 7(b), where the reflection amplitudes are almost the same and the imbalance of the reflection phase is about 1.3 degrees when l changes from 2.4 to 4.0 mm. The stable properties of the phase-shifting surfaces at the low-frequency band indeed make them feasible to implement a FP cavity antenna. Besides, the reflection/

transmission amplitudes at the low-frequency band can be controlled by tuning the dimensions of the outer square loops of the FSS, which was described in detail in our previous work [8].
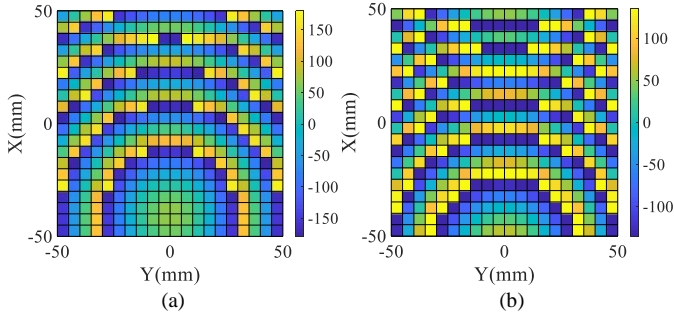

Fig. 8. Phase distribution on the plane of the phase-shifting surface. (a). At 26 GHz. (b). At 38 GHz.
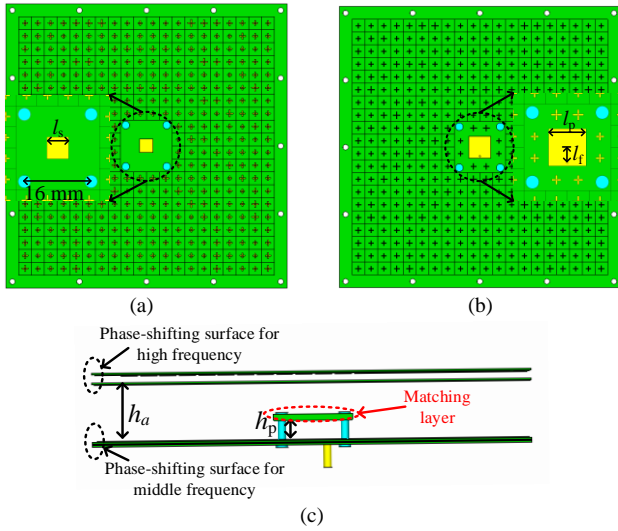

Fig. 9. The final model of the proposed triple-band shared-aperture antenna. (a). Front view of the matching layer. (b). Front view of the phase-shifting surface for middle frequency band, where a patch antenna operated at X-band is integrated into it. (c). Side view. (The feeding sources for middle and high frequency removed, l_s = 5. 2 mm, l_p = 8.6 mm, l_f = 3.5 mm.)

III. TRIPLE-BAND SHARED-APERTURE ANTENNA IMPLEMENTATION

In this section, the proposed triple-band shared-aperture antenna is implemented based on the proposed UCs. For demonstration, both the phase-shifting surfaces for middle and high-frequency bands are composed of 400 UCs (20 × 20 UCs) considering the compromise between the realized gains and simulation time. As seen from the schematic diagram in Fig. 1, the positions of the feeding sources for middle and high frequency are associated with the air separation h_a. The value of h_a is calculated by using the following formula:

$$-2\frac{2\pi}{c}fh_a - \varphi_{PSH} - \varphi_{PSM} = 2n\pi, n = 0, \pm1, \pm2, \pm3,... \quad (1)$$

where φ_{PSH} and φ_{PSM} are reflection phases of the phase-shifting surfaces for the high and middle frequency at the low-frequency band, respectively, as can be obtained from Fig. 7. c is the light velocity, and f is the frequency of interest. Using Eq. (1), the value of h_a equals 15.0 mm when f is 9.0 GHz.

In order to decrease the blockage effects of the feeding sources, the off-set feeding technique is adopted as shown in Fig. 1, where the feeding sources are located at the two sides of the phase-shifting surfaces. We select an ultra-wideband and linearly-polarized commercial horn antenna with a small footprint as the feeding source for both middle- and high-frequency bands to further minimize its blockage. Its gains and beamwidths with frequencies are fixed for the horn antenna, which can be obtained by simulating its model with CST software and verified by experimental measurements. In our design, the sizes of the phase- shifting surfaces and beamwidths of the horn antenna are known, while the height and offset angle of the feeding sources need to be determined, where the illumination coverage and the edge/corner element effect can be evaluated accordingly. In [18], the authors claimed that a better efficiency is usually obtained when the feeding beam is directed to a point between the aperture center and the bisecting point of the aperture angle. After some trial and error simulations, the optimal positions (height and offset angle) of the feeding sources are listed as follows: x_m = 50 mm, z_m = 60 mm, φ_1 = 36°, x_h = 55 mm, z_h = 110 mm, φ_2 = 30°.

Once the positions of the feeding sources are determined, the phase distributions on the planes of the phase-shifting surfaces can be obtained at 26 and 38 GHz, which are plotted in Fig. 8. Besides, the illumination coverages can also be evaluated by checking the electric field distributions on the planes of the phase-shifting surfaces. The electric field at the edge element is around 12dB lower than the peak electric field at 26 and 38 GHz, which is common value in reflectarray and transmitarray antenna designs. For very few corner elements, the electric field is around 14 dB lower than the peak value at 26 and 38 GHz. Such illumination coverages of the phase-shifting surfaces contribute to the sidelobe level of the proposed antenna at the middle- and high-frequency bands, which will be demonstrated from the radiation patterns at 26 and 38 GHz. Based on the phase distributions, the phase-shifting surfaces are implemented by the proposed UCs.

From Fig. 1, the feeding source for low frequency should locate between the two phase-shifting surfaces. Here, the feeding source is integrated into the phase-shifting surfaces for middle frequency as shown in Fig. 9, where a square patch is properly sized to make it work at 9 GHz. The inner and outer radius of the coaxial cable to excite the square patch are 0.27 and 0.81 mm, respectively.

For such a square patch antenna, the movement of the feeding point (l_f) is a widely-used technique to optimize the impedance match and reflection coefficient. However, for the FP cavity antenna in the proposed triple-band shared-aperture antenna, the patch antenna only serves as a feeding source, both the phase-shifting surfaces affect the input impedance of the FP cavity antenna. The simulations reveal that the movement of the feeding point (l_f) and resizing the square patch are not able to improve the impedance match and reflection coefficient. Here, a matching layer (ML) located above the square patch (as shown in Fig. 9 (c)) is introduced to improve the impedance match. The substrate of the matching layer is a 1.524 mm-thick Rogers RO4003C. Fig. 10 gives the reflection coefficient of the proposed triple-band shared-aperture antenna from 8 to 10 GHz. It is observed that the use of the ML improves the impedance match significantly. Moreover, the reflection coefficient can also be tuned by adjusting the value of h_p. The mechanism of the ML be able to improve the impedance match at the low-frequency band can be explained from the equivalent circuit and input impedance. The approximate equivalent circuit of the ML is shown in the inset of Fig. 10(b), where the square metal patch contributes to the inductor. As the electrical lengths of the air space (h_p) and 1.524mm-thick substrate are much smaller than the wavelength at 9.0 GHz, the input impedance of the equivalent circuit can be inductive. The inductive impedance can compensate for the original capacitive impedance to modify the input impedance as observed in Fig. 10 (b), thereby improving the impedance match of the proposed triple-band shared-aperture antenna at the low-frequency band. It

should be mentioned here that even though the ML is introduced, Eq.(1) still holds to calculate h_a as the size of the ML is much smaller than the phase-shifting surfaces and most of the electromagnetic waves still experience multiple reflections among the phase-shifting surfaces.
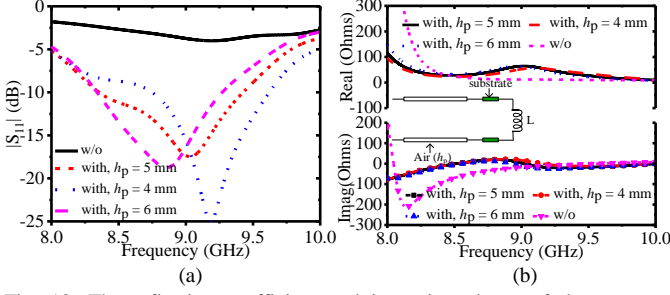

Fig. 10. The reflection coefficient and input impedance of the proposed triple-band shared-aperture antenna at the low-frequency band. (a). Reflection coefficient. (b). Input impedance.
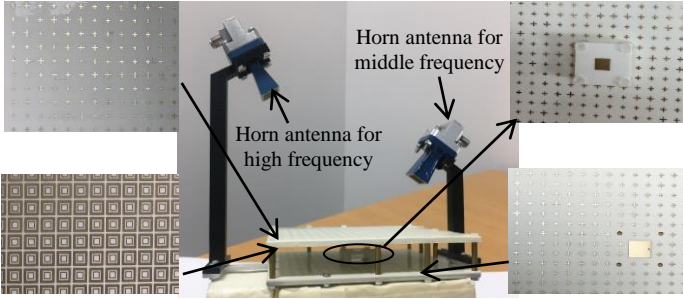

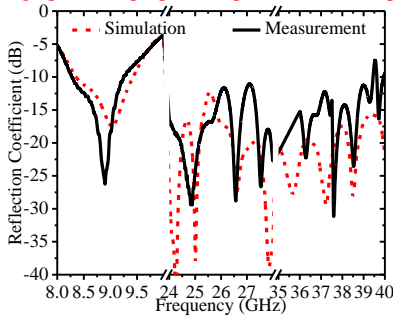Fig. 11. The photograph of the proposed triple-band shared-aperture antenna.

Fig. 12. Measured and simulated reflection coefficients of the proposed shared-aperture antenna at three different frequency bands.
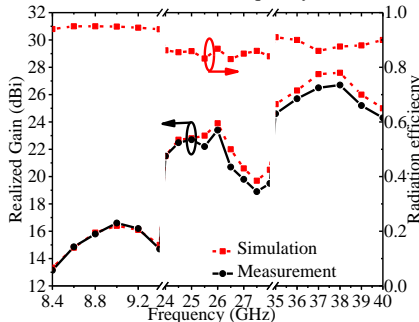

Fig. 13. Measured and simulated realized gains, and simulated radiation efficiency of the proposed shared-aperture antenna at three frequency bands.

IV. MEASUREMENT AND DISCUSSIONS

In this section, the proposed triple-band shared-aperture antenna has been fabricated and measured. All boards are produced with printed circuit board (PCB) technologies. Sixteen air holes with a diameter of 2 mm are drilled and distributed uniformly on the edges of every board for alignments. Fig. 11 shows the photograph of the proposed triple-band shared-aperture antenna and different board layers.

A. S-Parameters.

The S-parameters of the proposed triple-band shared-aperture antenna are measured with Keysight N5227A Power Network Analyzer (PNA). The measured reflection coefficients at the low-, middle-, and high-frequency bands are shown in Fig. 12, where the simulated results are also plotted for comparison. As seen in Fig. 12, the measured and simulated results agree with each other. The measured reflection coefficients below -10 dB from 8.25 to 9.3 GHz, 24 to 28 GHz, and 35 to 40 GHz are demonstrated. The reflection coefficient at around 39.5 GHz is slightly higher than -10 dB, which is mainly due to the effects of the coaxial to waveguide transition instead of the proposed antenna itself.

B. Realized gain and radiation patterns

According to the measured reflection coefficients, the realized gains and radiation patterns are measured in our anechoic chamber. It should be mentioned that when one port is excited, the remaining ports operating at other frequency bands should be terminated with matching loads. As seen in Fig. 13, the measured and simulated realized gains of the proposed triple-band shared-aperture antenna at the low-frequency band are highly consistent, achieving a peak gain of 16.8 dBi at 9 GHz. The 11.2% 3dB gain bandwidth (from 8. 4 to 9.4 GHz) mainly attributes to the wide bandwidth of the partial reflection/ transmission and proper reflection phases of the phase-shifting surfaces at the low-frequency band. In contrast, the measured realized gains at the middle and high-frequency bands are slightly smaller (less than 1.0 dB) than the simulated results. The aperture efficiency of the proposed antenna is 41.4 % at 9.0 GHz, 26.0 % at 26 GHz, and 29.2 % at 38 GHz, respectively. The gain drop beyond 26 GHz at the middle-frequency band mainly attributes to the oblique incidence effects of the UCs. The relatively big difference between the simulated and measured results at the high-frequency band is mainly due to the non-constant distance between the layers of the phase-shifting surface for high frequency (as shown in Fig. 9(c)) since there exists a slight bending and the air space (h_a) is not exactly equal to 15.0 mm in the antenna assembling. The simulated radiation efficiency of the proposed antenna is also presented in Fig. 13, where above 85 % radiation efficiency can be observed over the three bands.

The radiation patterns of the proposed triple-band shared-aperture antenna are measured. Fig. 14 presents the measured normalized radiation patterns at 9.0, 26.0, and 38.0 GHz, where the simulated counterparts are also plotted for comparison. As seen in Figs. 14 (a) and (b), the measured co-polarization (co-pol) in E- and H-plane is highly consistent with the simulated result. The measured cross-polarization (cro-pol) in E- and H-plane is below -40 and -20 dB, respectively. At 26.0 GHz, the measured co-polarization (co-pol) radiation patterns in E- and H-plane agree with the simulated results. As seen in Figs. 14 (c) and (d), the measured sidelobes are -18 and -20 dB in E- and H-plane, respectively; and the measured cross-polarization (cro-pol) levels are below -35 and -20 dB in E- and H-plane, respectively. The measured and simulated co-polarization (co-pol) radiation patterns in E- and H-plane have a good agreement with each other at 38.0 GHz. From Figs. 14 (e) and (f), the measured sidelobes are -19 and -20 dB in E- and H-plane, respectively; and the measured cross-polarization (cro-pol) levels are below -30 and -20 dB in E- and H-plane, respectively.

The performance of the proposed antenna with other similar and state-of-the-art work is compared as shown in Tab. I. The proposed antenna is highlighted by its higher operating bands, possibility of dual/circular polarization, simple configuration to achieve a high gain, and high aperture reuse efficiency since the FP cavity antenna makes full use of the phase-shifting surfaces for middle- and high-frequency bands. As the frequency responses of the proposed antenna are highly independent among three operating bands, the frequency ratio of the

proposed antenna can be flexibly controlled by choosing the proper dimensions of the FSSs and phase-shifting unit cells.
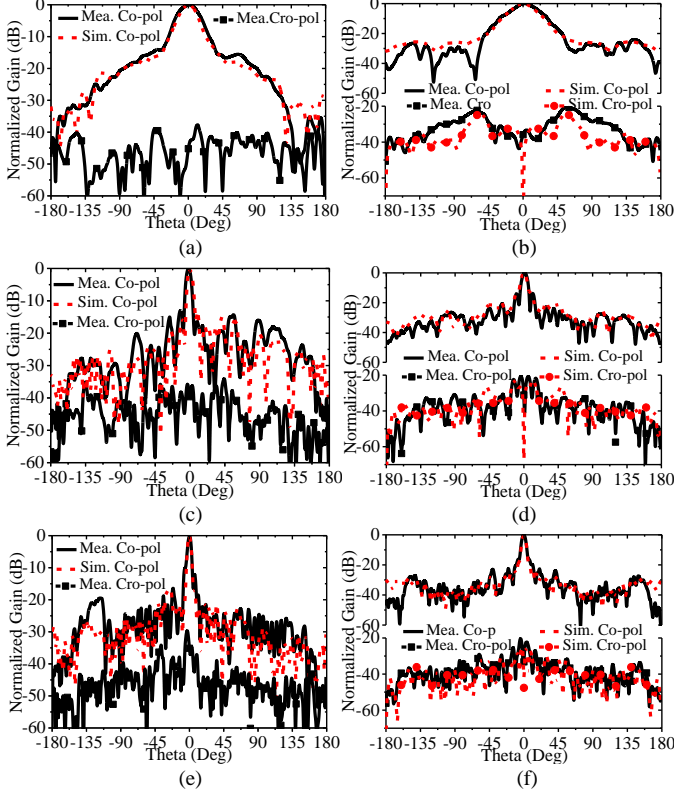

Fig. 14. Measured and simulated normalized realized gains of the proposed shared-aperture antenna. E-plane at: (a) 9.0 GHz, (c) 26.0 GHz, and (e) 38.0 GHz. H-plane at: (b) 9.0 GHz, (d) 26.0 GHz, and (f) 38.0 GHz.

Table. I. Comparison of the proposed antenna with other state-of-the-art triple-band shared-aperture antennas

Ref.	O_B, BW (GHz)	Gain (dBi)	R_E	F_R	ARE	Complex.
[11]	9.45-9.8, 3.6% 14.6-15.6, 6.7% 33-34.75, 5.3%	13.8 18.1 19.2	> 80%	1: 1.57: 3.52	L	H
[12]	1.56-1.94, 21.7% 3.08-3.46,11.6% 8.65-10.45,18.9%	6.3 14.0 21.0	N.A	1: 1.87: 5.46	L	H
#[13]	1.65-2.7, 50.2% 3.26-3.72, 13.1% 4.4-5.36, 17.5%	14.8 17.8 19.1	N.A	1: 1.60: 2.24	M	H
Pro.	***8.4-9.4, 11.2%** **24-26.6, 10.0%** **35-40, 13.3%**	**16.8** **23.8** **26.7**	**> 85%**	**1: 2.84: 4.21**	**H**	**S**

O_B: operating band; BW: bandwidth; R_E: radiation efficiency; F_R: frequency ratio; ARE: aperture reuse efficiency; H: high; M: moderate; L: low; S: simple. #: 1×4 antenna array; *: 3dB gain bandwidth. Complex: complexity.

V. CONCLUSIONS

A triple-band shared-aperture antenna with high figures of merit is described in this communication. A FP cavity antenna operated at X-band is integrated into a dual-band reflectarray antenna operated at K- and Ka-band to form the proposed antenna. By properly designing the phase-shifting surfaces for K- and Ka-band, the controls of the frequency responses of the proposed antenna can be highly independent at three operating bands. For proof of the concept, a prototype has been designed, fabricated, and measured. It presents the 3-dB gain bandwidths of 11.2 % (8.4 to 9.4 GHz), 10 % (24 to 26.6

GHz), 13.3 % (35 to 40 GHz), and the peak gains of 16.8 dBi at 9.0 GHz, 23.8 dBi at 26 GHz, 26.7 dBi at 38 GHz. Good agreement with the simulated results has been observed.

REFERENCES

[1] L. Kong, and X. Xu, "A compact dual-band dual-polarized microstrip antenna array for MIMO-SAR applications," *IEEE Trans. Antennas and Propag.*, vol. 66, no. 5, pp. 2374-2381, May. 2018.

[2] J. Zhang, W. Wu, and D. Fang, "Dual-band and dual-circularly polarized shared-aperture antenna with single-layer substrate," *IEEE Trans. Antennas and Propag.*, vol. 64, no. 1, pp. 109-116, Jan. 2016.

[3] T. Li, and Z. N. Chen, "Shared-surface dual-band antenna for 5G applications," *IEEE Trans. Antennas and Propag.*, vol. 68, no. 2, pp. 1128-1133, Feb. 2020.

[4] T. Li, and Z. N. Chen, "Metasurface-based shared-aperture 5G S-/K-Band antenna using characteristic mode analysis," *IEEE Trans. Antennas and Propag.*, vol. 66, no. 12, pp. 6742-6750, Dec. 2018.

[5] J. Zhang, Y. Cheng, Y. Ding, and C. Bai, "A dual-band shared-aperture antenna with large frequency ratio, high aperture reuse efficiency, and high channel isolation," *IEEE Trans. Antennas and Propag.*, vol. 67, no. 2, pp. 853-860, Feb. 2019.

[6] Y. Ding, and Y. Cheng, "Ku/Ka dual-band dual-polarized shared-aperture beam-scanning antenna array with high isolation," *IEEE Trans. Antennas and Propag.*, vol. 67, no. 4, pp. 2413-2422, Apr. 2019.

[7] Y. Chen, J. Zhao, and S. Yang, "A novel stacked antenna configuration and its applications in dual-band shared-aperture base station antenna array designs," *IEEE Trans. Antennas and Propag.*, vol. 67, no. 12, pp. 7234-7241, Dec. 2019.

[8] P. Mei, S. Zhang, and G. F. Pedersen, "A dual-polarized and high-gain X/Ka-band shared-aperture antenna with high aperture reuse efficiency," *IEEE Trans. Antennas and Propag.*, vol. 69, no. 3, pp. 1334-1344, Mar. 2021.

[9] R. S. Malfaiani, and Z. Atlasbaf, "Design and implementation of a dual-band single layer reflectarray in X and Ka bands," *IEEE Trans. Antennas and Propag.*, vol. 62, no. 8, pp. 4425-4431, Aug. 2014.

[10] T. Smith, U. Gothelf, O. Kim, and O. Breinbjerg, "An FSS-backed 20/30 GHz circularly polarized reflectarray for a shared-aperture L- and Ka-band satellite applications," *IEEE Trans. Antennas and Propag.*, vol. 62, no. 2, pp. 661-668, Feb. 2014.

[11] C. Mao, S. Gao, Q. Luo, T. Rommel, and Q. Chu, "Low-cost X/Ku/Ka-band dual-polarized array with shared aperture," *IEEE Trans. Antennas and Propag.*, vol. 65, no. 7, pp. 3520-3527, Jul. 2017.

[12] K. Li, T. Dong, and Z. Xia, "A broadband shared-aperture antenna L/S/X-band dual-polarized antenna for SAR applications," *IEEE Access*, vol. 7, pp. 51417-51425, June. 2019.

[13] G. Zhou, B. Sun, Q. Liang, S. Wu, Y. Yang, and Y. Cai, "Tri-band dual-polarized shared-aperture antenna for 2G/3G/4G/5G base station application," *IEEE Trans. Antennas and Propag., Early Access.*, vol. 69, no. 1, pp. 97-108, Jan. 2021.

[14] R. Deng, F. Yang, S. Xu, and M. Li, "An FSS-backed 20/30-GHz dual-band circularly polarized reflectarray with suppressed mutual coupling and enhanced performance," *IEEE Trans. Antennas and Propag.*, vol. 65, no. 2, pp. 926-931, Feb. 2017.

[15] M. R. Chaharmir, and J. Shaker, "Design of a multilayer X-/Ka-band frequency-selective surface-backed reflectarray for satellite applications," *IEEE Trans. Antennas and Propag.*, vol. 63, no. 4, pp. 1255-1262, Apr. 2015.

[16] P. Mei, S. Zhang, X. Q. Lin, and G. F. Pedersen, "Design of an absorptive Fabry-Perot polarizer and its application on antenna," *IEEE Antennas Wireless Propag. Lett.*, vol. 18, no. 7, pp. 1352-1356, July. 2019.

[17] N. Nguyen-Ttong, H. Tran, T. Nguyen, and A. Abbosh, "Wideband Fabry-Perot antennas employing multilayer of closely spaced thin dielectric slabs," IEEE Antennas Wireless Propag. Lett., vol. 17, no. 7, pp. 1354-1358, July. 2018.

[18] A. Yu, F. Yang, A. Z. Elsherbeni, J. Huang, and Y. Rahmat-Samii, "Aperture efficiency analysis of reflectarray antennas," Microwave and Optical Tech Lett, vol. 52, no. 2, pp. 364-372, Feb 2010.